Supplementing a survey of geosynchronous debris with commercial-off-the-shelf equipment

James A. Blake, Paul Chote, Don Pollacco, Dimitri Veras
Astronomy & Astrophysics Group, University of Warwick, UK
Andrew Ash, William Feline, Grant Privett
Defence Science & Technology Laboratory, UK

Laura Pirovano
Auckland Space Institute, University of Auckland, NZ

ABSTRACT

Recent anomalies and break-ups by satellites and rocket bodies have added more fragments to an already substantial population of debris in high-altitude Earth orbits. Many of these fragments are too faint to detect with small telescopes, instead requiring the superior collecting area of larger instruments.

Optical surveys of the geosynchronous (GSO) region typically undergo a balancing act between sky coverage, survey depth and cost. Large survey areas can be achieved at a reasonable cost using commercial-off-the-shelf (COTS) components, but these systems are limited to apertures around 30 cm in size. Large telescopes, with apertures exceeding 1 m, can probe the faint debris population to uncover objects at the decimetre level, but usually suffer from a small field of view ($\lesssim$ 1 square degree) and are not available commercially at scale. As a consequence, surveys attempting to probe the faint debris population with large telescopes are often limited to targeted observations of known fragmentation events. Otherwise, a small field of view coupled with a desire to cover more sky can result in very sparse or limited positional information for the objects detected.

In this paper, we explore the benefits of pairing a large telescope with a COTS instrument in the context of a blind survey of the GSO region. We utilise a dataset acquired in September 2018 by a 36 cm robotic astrograph, whilst synchronised to the 2.54 m Isaac Newton Telescope in La Palma, Canary Islands. We exploit the larger field of view of the COTS instrument to supplement the bright end of the sampled population. The shorter readout time for the astrograph reduces the deadtime between exposures and therefore enables the extraction of better-quality photometric light curves for brighter detections.

This study forms part of DebrisWatch, an ongoing collaboration between the University of Warwick and the Defence Science and Technology Laboratory (UK) investigating the population of GSO debris. The work presented will prelude a wider comparative analysis between the two available datasets.

1. INTRODUCTION

Artificial satellites in geosynchronous Earth orbit (GSO) continue to play an integral role in service provision for a whole host of applications. Unique properties of GSO satellites, such as the localised nature of their ground tracks and their ability to provide expansive coverage, have been exploited for telecommunications, weather monitoring and navigation since the formative years of the Space Age. The high cost associated with manufacturing, launching and operating a GSO satellite, coupled with the limited number of viable orbital slots, warrants a more comprehensive understanding of the region's debris environment.

Observations of recent anomalies and break ups in the vicinity of the GSO region have highlighted the existence of a population of small debris in high-altitude orbits [1, 2]. The majority of these fragments are too faint to be routinely tracked and monitored by the Space Surveillance Network (SSN) [3]; a concern, given that a significant proportion of the fragments cross the GSO Protected Region, posing a direct threat to active satellites.

Many surveys [see e.g. 4–8] of the GSO region have been conducted using optical telescopes with diameters 1 m or less, typically achieving sensitivity limits in the range 15^{th}–20^{th} Magnitude. The cited surveys have uncovered a few

Table 1: Specifications of interest for the instruments used. Note that the quoted field of view (FOV) for the Wide Field Camera (WFC) is lower than its achievable 34 sq. arcmins, owing to severe pickup noise that rendered one of the CCD chips unusable.

Instrument	Aperture [m]	CCD(s) [px]	FOV	Resolution [$''$px^{-1}]	Readout time [s]	Filter
INT WFC	2.54	4×2k×4k (mosaic)	$33' \times 22'$	0.66 (binned, 2×2)	25	Harris *V*
RASA	0.36	8k×6k	$3.6^\circ \times 2.7^\circ$	1.57 (unbinned)	4	None

thousand fragments of sub-1 m debris in high-altitude orbits, in some cases probing to the 15-20 cm level (depending on the assumed phase angle, shape and albedo). A few surveys [9–11] have probed deeper with larger telescopes, which typically have a small field of view. This can act to the detriment of the survey in one of two ways: targeted observations of known fragmentation events can be performed at the expense of poor sky coverage, or wider-reaching pointing strategies can be employed, resulting in sparse or limited positional information for the objects detected.

The latter was true for a survey of the GSO region conducted with the 2.54 m Isaac Newton Telescope (INT) in September 2018 [11, 12]. Here, we present a preliminary analysis of a supplementary dataset acquired by a commercial-off-the-shelf (COTS) instrument that was synchronised to the INT for the duration of the survey. We provide an overview of our instrumentation and chosen observational strategy in Sec. 2, before outlining the latest version of our custom analysis pipeline in Sec. 3. In Sec. 4, we explore the ways in which the paired COTS instrument alleviates some of the limitations associated with deep GSO surveys, and discuss plans for a wider comparative analysis of the available datasets.

2. INSTRUMENTATION AND OBSERVATIONAL STRATEGY

Simultaneous observations were carried out using the 2.54 m INT and a COTS robotic instrument, both situated within the Roque de los Muchachos Observatory on the Canary Island of La Palma. Photometric analyses undertaken for the INT dataset were presented previously in [11], and we refer the interested reader to this study for further detail regarding the observational strategies used.

The COTS instrument (hereafter RASA) made use of a 36 cm Rowe-Ackermann Schmidt astrograph and an FLI ML50100 camera, and was temporarily installed on a Paramount ME mount for the duration of a separate survey accruing light curves for catalogued GSO targets [13]. The system featured a custom GPS timestamping unit enabling precise start- and end-of-exposure times to be measured. We provide key specifications for the instruments used in Table 1.

The observations span eight nights of dark-grey time from 2–9 September 2018. Target fields were selected based on their proximity to the Earth's shadow, leading or trailing the shadow in order to minimise the solar phase angle (observatory-target-Sun) and thus maximise the apparent brightness of candidate GSO objects. Images were acquired with the telescopes fixed in the topocentric coordinate frame (i.e. 'stopped', not tracking) to ensure that photons from potential GSO candidates would integrate over fewer pixels during the exposure. An exposure time of 10 s was chosen as a compromise on the observational duty cycle, and also to limit star coverage in the CCD frames (stars streak across the images at the sidereal rate in our mode of operation).

In Fig. 1, we show the declination strips mapped out by the RASA pointings over the course of the survey. Multiple exposures were taken per pointing to allow for detections to be correlated between successive frames. The reduction in deadtime afforded by the shorter readout and slew times of the RASA allowed for more exposures to be acquired at each pointing. For every sequence of seven exposures undertaken by the INT, typically 20–25 were obtained with the RASA.

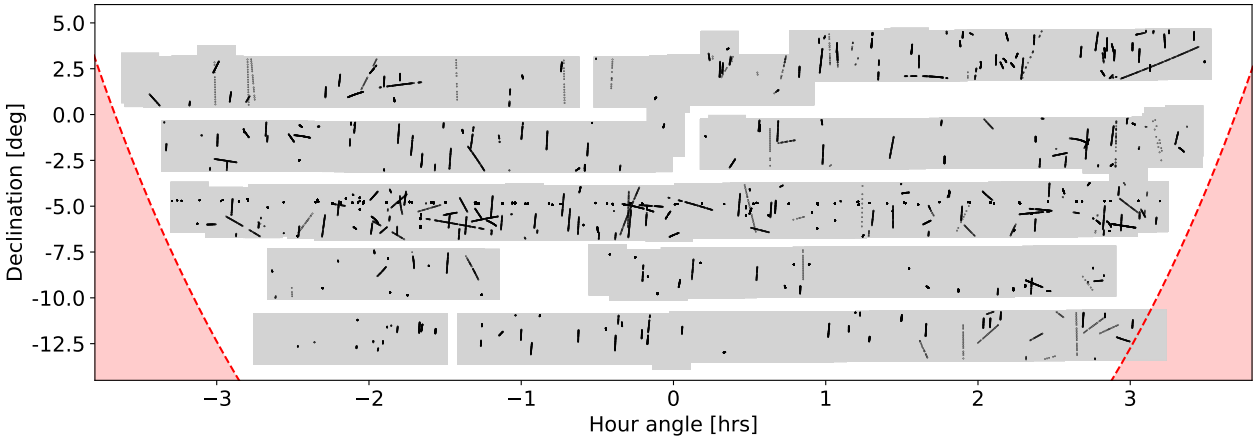

Fig. 1: Telescope pointings comprising the RASA dataset. Imaged fields are shaded in grey, while the black dots map out detections of candidate GSO objects uncovered by the analysis pipeline outlined in Sec. 3. The regions shaded in red denote the 30° altitude limits constraining the pointings of the INT.

3. ANALYSIS PIPELINE

We adapt the custom analysis pipelines presented in [11, 13] to process and reduce the raw CCD frames acquired by the RASA. We provide a brief overview of the key steps performed below, highlighting new developments, and refer the interested reader to the cited studies for further detail.

The pipelines employ a number of existing astronomical packages, including `SEP` [14, 15], `Astrometry.net` [16], `astropy` [17, 18], `astroquery` [19], `scipy` [20] and `photutils` [21]. Prior to the frame-by-frame processing, master calibrations are generated from bias and flat field frames taken at the start and end of each night. We then utilise the available metadata for each frame of a given night to ascertain an appropriate search box for a bulk query to the *Gaia* DR2 catalogue, resulting in a local database of comparison stars for photometric calibration. We opt to calibrate the RASA frames in the *Gaia G* band, in order to best approximate the lack of filter.

Each frame is subsequently processed as follows:

- Bias and flat field calibrations are applied, and a model of the spatially varying sky background is subtracted from the calibrated frame.
- Star trails are extracted from the frame by exploiting their common morphologies, and subsequently used to obtain a preliminary astrometric solution.
- Comparison stars are queried from the local database and filtered to reject those that are blended or saturated. The star trails in the frame are then cross-matched with the surviving comparisons to obtain a photometric zero point. A brightness cut is applied to filter out anomalous matches.
- The astrometric solution is refined using an adaptation of the algorithm described in [13]. A custom 2D distortion map is fitted and an iterative improvement of the cross-match is carried out. As shown in Fig. 2, the implementation of this technique has greatly improved the quality of the resulting astrometric solution.
- Mathematical morphology techniques [see e.g. 22, 23] are applied to remove the star trails. A threshold-based source extraction is then performed on the star-subtracted frame. We map the 'known' positions of the *Gaia* comparison stars to the image space using the astrometric solution and carry out a proximity check, filtering out common false positives that survive the star subtraction.
- Aperture photometry is performed for the surviving detections. An estimate of total brightness is obtained by summing the contents of a circular aperture if the detection is point-like (geostationary) or those of a rectangular aperture if the detection is trailed in the image.

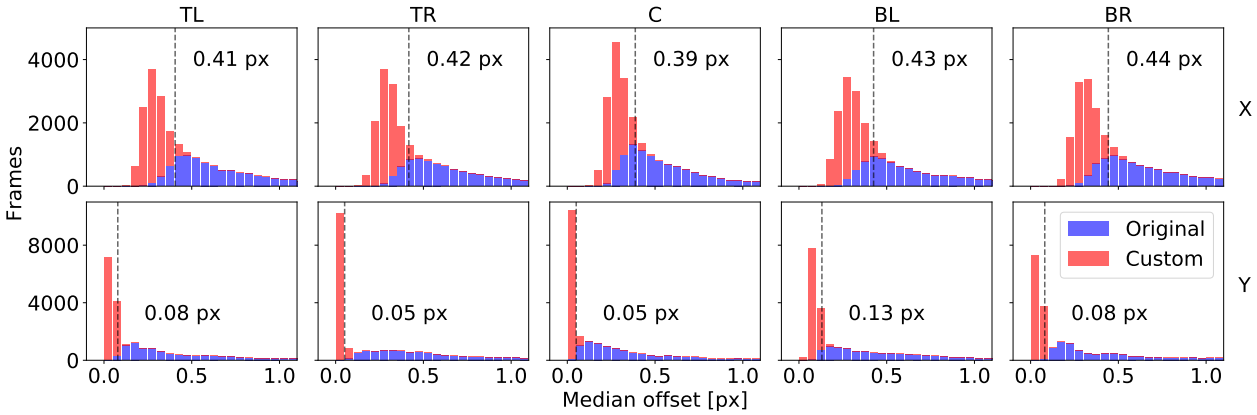

Fig. 2: Astrometric accuracies achieved using Astrometry.net (blue) and the custom algorithm described in Sec. 3 (red). The top panels show median offsets in the X (right ascension) direction between the detected star trails and their matched comparisons, while those in the bottom panels correspond to the Y (declination) direction. We consider the median offset for matched stars within a 2044 px×2044 px tile situated in the top left (TL), top right (TR), centre (C), bottom left (BL) and bottom right (BR) regions of a given frame. In each panel, we label the 95$^{\text{th}}$ percentile achieved by the custom algorithm. Owing to the trailed nature of the stars in our images, we see a better performance in declination than in right ascension.

The processed frames are subsequently used to carry out the following tasks:

- Candidate objects of interest are correlated between the individual frames of a given pointing of the telescope, by fitting and sequentially updating a linear trajectory. Trails comprising multiple detections within a single exposure (e.g. those exhibiting signs of tumbling) are identified at this stage and combined to generate an estimate of the overall centroid. These cases undergo additional vetting by eye. Remaining false positives are discarded as single detections; we require a detection to be found in two or more frames to be considered in the analyses that follow.
- Light curves are extracted for off-geostationary cases by placing rectangular apertures along the trail, making use of the fitted trajectory to map spatial position to time. Reference images are used to subtract out contaminating background sources (e.g. star trails).

4. RESULTS AND DISCUSSION

In the top-left panel of Fig. 3, we display brightness histograms for the short arcs detected by the INT and the RASA. The higher detection rate for the RASA is immediately clear, owing to its wider coverage. A total of 1205 arcs comprising two or more detections within a given pointing were extracted from the RASA observations, compared to 226 arcs from those of the INT. However, the inferior sensitivity of the RASA drops off at around $G \sim 16.5$, so only the bright end of the sampled population is supplemented by the COTS instrument.

We find the bright end of the RASA distribution to be split into two peaks. The first, centred around $G \sim 10.5$, corresponds to station-kept geostationary satellites that appear as points in the CCD images. Such objects were found to easily saturate in a typical 10 s INT exposure, owing to its superior sensitivity. The RASA observations offer a chance to correct for the resulting skew at the extreme bright end of the distribution. A second peak is visible around $G \sim 12.5$, consistent with several other surveys undertaken at a similar longitude [see e.g. 7]. This peak likely corresponds to former geostationary satellites that have been retired to graveyard orbits, as per the recommended guidelines [see 24]. Owing to a lack of attitude control beyond decommisioning, many of these satellites exhibit a tumbling motion that is dependent on the perturbative forces acting within the local GSO region. Satellites that are tumbling in this way will brighten and fade as highly-reflective components (e.g. solar panels) pass in and out of an observer's line of sight, hence the discrepancy in average brightness between the two peaks.

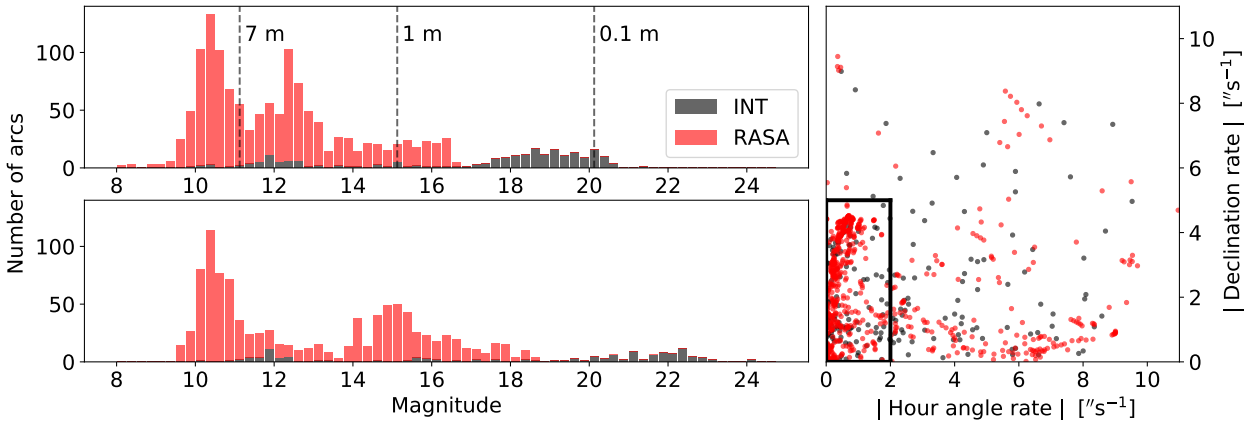

Fig. 3: Top left) Histogram of brightness measurements for the full sample of orbital arcs detected by the INT (black) and the RASA (red) over the course of the survey. It is important to note that separate band passes were used to calibrate the brightness measurements for each instrument, in light of the different filters used (see Table 1). The term 'Magnitude' thus refers to calibrated APASS V magnitude for the INT detections, and calibrated Gaia G magnitude for the RASA detections. The translational offset attributed to this colour term is of the order of +0.5 mag for the RASA measurements (i.e. towards fainter magnitudes), and is not applied here. Annotated size estimates are provided as a rough guide, and assume that the corresponding objects are Lambertian spheres with an albedo of 0.1. Right) Angular rates in hour angle and declination for the objects detected by the INT (black) and the RASA (red). We apply rate cuts (black box) to filter the sample to include only objects that likely reside in circular GSOs. Bottom left) Histogram of brightness measurements for the circular GSO sample of orbital arcs detected by the INT (black) and the RASA (red), normalised by trail length.

As shown in the right panel of Fig. 3, we apply rate cuts to obtain a sample of arcs corresponding to GSO objects that likely reside in circular orbits. We enforce that $|$ Hour angle rate $| < 2''\mathrm{s}^{-1}$ and $|$ Declination rate $| < 5''\mathrm{s}^{-1}$, as in [25]. The rate cuts reduce the sample size to 956 arcs for the RASA and 129 arcs for the INT.

For the resulting circular GSO sample, we plot an additional histogram in the bottom-left panel of Fig. 3, having normalised the brightness measurements by a factor x/l, where x is characteristic of the point spread function of the optical system and l is the length of the path traversed over the course of the exposure. This gives the brightness of a point-like source possessing an equivalent peak flux for the same integration time, and so provides a clearer representation of the detection capabilities of the sensor. In the normalised regime, the peak centred on $G \sim 10.5$ remains largely unchanged, reinforcing the interpretation that it corresponds to the geostationary targets that are point-like and consequently unaffected by the normalisation. Conversely, the majority of arcs making up the second peak appear to exhibit off-geostationary motion, as they shift towards fainter magnitudes, again reinforcing our previous interpretation that they correspond to objects in graveyard orbits.

In Fig. 4, we provide examples of simultaneous light curves extracted from the INT and RASA observations. Photometric light curves form a useful byproduct of GSO surveys, and contain information pertaining to the shape, reflectivity and attitude of the corresponding object. The development of techniques to extract this information from photometric data is an active area of research [see e.g. 26–28], with some surveys dedicating their efforts to providing high-quality test data [e.g. 13, 29].

The top two panels of Fig. 4 give the light curves for two SL-12 rocket bodies: NORAD 16797 and NORAD 15581, respectively. We see a superb agreement between the INT and RASA photometry when considering brightness variability, accounting for the roughly 0.5 mag offset that we attribute to a colour term introduced by the differing filter responses. Although the RASA was scripted to observe the same fields as the INT, the exposures themselves were not synchronised. As a result, we find that the RASA observations act to fill the gaps in the INT light curves. The improved duty cycle of the RASA (resulting from reduced readout and field acquisition overheads) is clearly beneficial, allowing measurements to be made across a larger proportion of the observation window, and extending the window for each individual pointing.

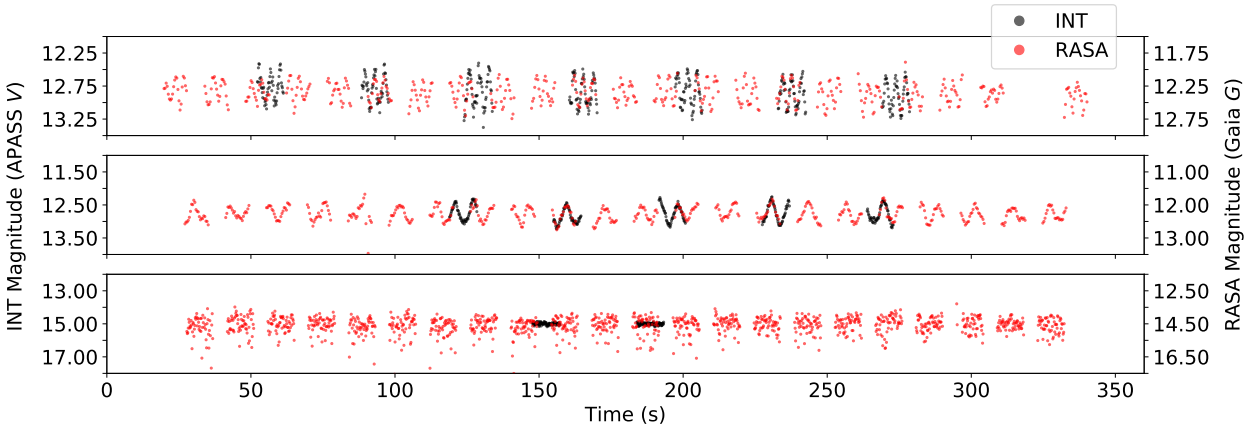

Fig. 4: Examples of simultaneous light curves obtained with the INT (black) and the RASA (red). We find an offset of roughly 0.5 mag between the two instruments, a colour term that we attribute to the different band passes used for photometric calibration. The light curves given in the top and middle panels correspond to orbital arcs correlated with SL-12 rocket bodies NORAD 16797 and NORAD 15581, respectively. The bottom panel shows the light curve extracted for an orbital arc that failed to correlate with the publicly-available USSTRATCOM catalogue.

The light curve in the bottom panel of Fig. 4 corresponds to an uncorrelated arc. Here, the limitations of the RASA's sensitivity become apparent. A higher degree of scatter can be seen in the RASA brightness measurements compared to those of the INT, owing to the lower signal to noise of the sources within the corresponding frames. The signal to noise can be improved by binning data in the time domain, but this is subject to a trade-off with time resolution. In the top panel, we also see the effect of the larger pixel scale on time resolution for the RASA light curves, acting to diminish the amplitude of the oscillations.

In future development of the project, we aim to carry out a correlation between successive pointings to combine individual arcs belonging to the same object. Owing to its wider field, a given object is likely to remain in view of the RASA for multiple pointings as it slews in accordance with the INT. This will, in principle, extend the orbital arcs to cover 10–12 mins, compared to the 3–4 mins achievable with the INT observations. We aim to carry out initial orbit determination for the resulting collection of arcs using short arc techniques [30], to narrow down the number of unique objects surveyed.

5. SUMMARY

We have presented a preliminary analysis of simultaneous observations of the geosynchronous region undertaken by the 2.54 m Isaac Newton Telescope (INT) and a 36 cm commercial-off-the-shelf (COTS) robotic astrograph (RASA) across eight nights of dark-grey time in September 2018. Using adaptations of the custom analysis pipelines presented in [11, 13] to process the raw RASA CCD frames, we extract 1205 orbital arcs comprising two or more detections within a given pointing of the telescope, 956 of these exhibiting angular rates characteristic of objects in circular geosynchronous orbits. We uncover two dominant populations, the first centred around *Gaia* $G \sim 10.5$ corresponding to station-kept geostationary satellites, and the second centred around *Gaia* $G \sim 12.5$ which likely corresponds to satellites in graveyard orbits. The RASA's wider field of view acts to supplement the bright end of the sampled population, and facilitates extended coverage of the corresponding INT field prior to it passing out of view. For the brighter detections in the INT dataset, we are therefore able to extract longer orbital arcs by exploiting this feature of the RASA observations. We aim to carry out an initial orbit determination for these arcs in order to ascertain the number of unique objects surveyed. The reduced readout and field acquisition overheads afforded by the RASA allow for more extensive and complete light curves to be extracted from trailed detections. The larger pixel scale, however, leads to a reduction in time resolution compared to the light curves extracted from the INT observations. Overall, the simultaneous datasets have proved complementary in a variety of ways, and the use of the COTS instrument has been found to alleviate several limitations typically associated with large telescopes when conducting deep surveys of the geosynchronous region.

6. REFERENCES

[1] P. M. Cunio, M. Bantel, B. R. Flewelling, W. Therien, et al. Photometric and Other Analyses of Energetic Events Related to 2017 GEO RSO Anomalies. In *Proceedings of the Advanced Maui Optical and Space Surveillance (AMOS) Technologies Conference*, 2017.

[2] Thomas Schildknecht, Alessandro Vananti, Emiliano Cordelli, and Tim Flohrer. ESA optical surveys to characterize recent fragmentation events in GEO and HEO. In *Proceedings of the Advanced Maui Optical and Space Surveillance (AMOS) Technologies Conference*, 2019.

[3] D. S. McKnight and F. R. Di Pentino. New insights on the orbital debris collision hazard at GEO. *Acta Astronautica*, 85:73–82, 2013.

[4] F. Alby, M. Boer, B. Deguine, I. Escane, et al. Status of CNES optical observations of space debris in geostationary orbit. *Advances in Space Research*, 34(5):1143–1149, 2004.

[5] P. Seitzer, R. Smith, J. Africano, K. Jorgensen, et al. MODEST observations of space debris at geosynchronous orbit. *Advances in Space Research*, 34(5):1139–1142, 2004.

[6] E. Barker, K. Jarvis, J. Africano, K. Jorgensen, et al. The GEO environment as determined by the CDT between 1998 and 2002. In *4^{th} European Conference on Space Debris*, volume 587, page 135, 2005.

[7] T. Schildknecht. Optical surveys for space debris. *The Astronomy and Astrophysics Review*, 14(1):41–111, 2007.

[8] H. Luo, Y.-D. Mao, Y. Yu, and Z.-H. Tang. FocusGEO observations of space debris at Geosynchronous Earth Orbit. *Advances in Space Research*, 64(2):465–474, 2019.

[9] I. Molotov, V. Agapov, Z. Khutorovsky, V. Titenko, et al. Faint high orbit debris observations with ISON optical network. In *Proceedings of the Advanced Maui Optical and Space Surveillance (AMOS) Technologies Conference*, volume 21, 2009.

[10] P. Seitzer, E. Barker, B. Buckalew, A. Burkhardt, et al. The Population of Optically Faint GEO Debris. In *Proceedings of the Advanced Maui Optical and Space Surveillance (AMOS) Technologies Conference*, 2016.

[11] J. A. Blake, P. Chote, D. Pollacco, W. Feline, et al. DebrisWatch I: A survey of faint geosynchronous debris. *Advances in Space Research*, 2020. ISSN 0273-1177. doi: 10.1016/j.asr.2020.08.008.

[12] J. A. Blake, P. Chote, D. Pollacco, D. Veras, et al. Optical imaging of the geosynchronous region with the Isaac Newton Telescope. In *Proceedings of the Advanced Maui Optical and Space Surveillance (AMOS) Technologies Conference*, 2019.

[13] P. Chote, J. A. Blake, and D. Pollacco. Precision Optical Light Curves of LEO and GEO Objects. In *Proceedings of the Advanced Maui Optical and Space Surveillance (AMOS) Technologies Conference*, 2019.

[14] K. Barbary. SEP: Source Extractor as a library. *The Journal of Open Source Software*, 1(6):59, 2016.

[15] E. Bertin and S. Arnouts. SExtractor: Software for source extraction. *Astronomy and Astrophysics Supplement Series*, 117(2):393–404, 1996.

[16] D. Lang, D. W. Hogg, K. Mierle, M. Blanton, et al. Astrometry. net: Blind astrometric calibration of arbitrary astronomical images. *The Astronomical Journal*, 139(5):1782, 2010.

[17] T. P. Robitaille, E. J. Tollerud, P. Greenfield, M. Droettboom, et al. Astropy: A community Python package for astronomy. *Astronomy & Astrophysics*, 558:A33, 2013.

[18] A. M. Price-Whelan, B. M. Sipőcz, H. M. Günther, P. L. Lim, et al. The Astropy project: Building an open-science project and status of the v2. 0 core package. *The Astronomical Journal*, 156(3):123, 2018.

[19] A. Ginsburg, B. M. Sipőcz, C. E. Brasseur, P. S. Cowperthwaite, et al. astroquery: An Astronomical Web-querying Package in Python. *The Astronomical Journal*, 157(3):98, 2019.

[20] E. Jones, T. Oliphant, P. Peterson, et al. SciPy: Open source scientific tools for Python. 2001.

[21] L. Bradley, B. M. Sipőcz, T. Robitaille, E. Tollerud, et al. Photutils: Photometry tools. *Astrophysics Source Code Library*, pages ascl–1609, 2016.

[22] M. Laas-Bourez, G. Blanchet, M. Boër, E. Ducrotté, et al. A new algorithm for optical observations of space debris with the TAROT telescopes. *Advances in Space Research*, 44(11):1270–1278, 2009.

[23] E. J. Breen, R. Jones, and H. Talbot. Mathematical morphology: A useful set of tools for image analysis. *Statistics and Computing*, 10(2):105–120, 2000.

[24] IADC. Space debris mitigation guidelines. IADC-02-01, Revision 1, 6, 2007.

[25] P. Seitzer, S. M. Lederer, E. S. Barker, H. Cowardin, et al. A search for optically faint GEO debris. Technical report, National Aeronautics and Space Administration Houston TX Lyndon B. Johnson, 2011.

[26] R. Linares, M. K. Jah, J. L. Crassidis, and C. K. Nebelecky. Space object shape characterization and tracking using light curve and angles data. *Journal of Guidance, Control, and Dynamics*, 37(1):13–25, 2014.

[27] C. J. Benson, D. J. Scheeres, W. H. Ryan, E. V. Ryan, et al. GOES spin state diversity and the implications for GEO debris mitigation. *Acta Astronautica*, 167:212–221, 2020.

[28] S. Fan and C. Frueh. A direct light curve inversion scheme in the presence of measurement noise. *The Journal of the Astronautical Sciences*, 67(2):740–761, 2020.

[29] J. Šilha, S. Krajčovič, M. Zigo, J. Tóth, et al. Space debris observations with the Slovak AGO70 telescope: Astrometry and light curves. *Advances in Space Research*, 65(8):2018–2035, 2020.

[30] L. Pirovano, D. A. Santeramo, R. Armellin, P. Di Lizia, et al. Probabilistic data association: the orbit set. *Celestial Mechanics and Dynamical Astronomy*, 132(2):1–27, 2020.